ORIGINAL PAPER

Towards the Understanding of Sintering Phenomena at the Nanoscale: Geometric and Environmental Effects

F. Behafarid · B. Roldan Cuenya

Abstract One of the technologically most important requirements for the application of supported metal nanoparticles (NPs) to the field of heterogeneous catalysis is the achievement of thermally and chemically stable systems under reaction conditions. For this purpose, a thorough understanding of the different pathways underlying coarsening phenomena is needed. In particular, in depth knowledge must be achieved on the role of the NP synthesis method, geometrical features of the NPs (size and shape), initial NP dispersion on the support (interparticle distance), support pretreatment (affecting its morphology and chemical state), and reaction environment (gaseous or liquid medium, pressure, temperature). This study provides examples of the stability and sintering behavior of nanoscale systems monitored ex situ, in situ, and under *operando* conditions via transmission electron microscopy, atomic force microscopy, scanning tunneling microscopy, and X-ray absorption fine-structure spectroscopy. Experimental data corresponding to physical-vapor-deposited and micelle-synthesized metal (Pt, Au) NPs supported on TiO_2, SiO_2 and Al_2O_3 will be used to illustrate Ostwald-ripening and diffusion coalescence processes. In addition, the role of the annealing environment (H_2, O_2, water vapor) on the stability of NPs will be discussed.

Keywords Coarsening · Sintering · Ostwald-ripening · Diffusion-coalescence · Operando · Pt · Au · TiO_2 · SiO_2 · ZrO_2 · Al_2O_3 · Micelle · Nanoparticle · Environment effect · Interparticle distance · Size effect · Thermal stability · Encapsulation · Redispersion

F. Behafarid · B. Roldan Cuenya (✉)
Department of Physics, University of Central Florida, Orlando, FL 32816, USA
e-mail: roldan@ucf.edu

1 Introduction

Size-dependent changes in the binding of adsorbates [1, 2], enhanced activity [3–10], and distinct selectivity of nanoparticle (NP) catalysts as compared to their bulk counterparts have been reported. Significant attention has been dedicated to the study of sintering phenomena in nanoscale catalysts due to the detrimental effect that the concomitant loss of surface area has on the catalyst activity and durability [3, 11–18]. Thus, rationally engineering supported NP systems that guarantee the stability of their active elements in the course of a chemical reaction is fundamental in order to ensure their optimum performance in an industrial setting [19]. This review describes several parameters which are considered key players dominating the thermal and chemical stability of NP catalysts, namely, the NP geometry and arrangement (size, shape, interparticle distance) [20–24], NP synthesis method [25], support [23, 25–29], pre-treatment [30, 31], and environment [30, 32–39].

Two main sintering mechanisms have been commonly considered:[25, 40–46] (i) Ostwald-ripening, where atoms detach from small clusters and diffuse over the support surface until they find larger clusters, and (ii) diffusion-coalescence, where entire NPs diffuse across the support surface until they meet other NPs leading to coalescence. Numerous examples of both coarsening models can be found in the literature [20, 25, 27, 28, 30, 40–51], including the appearance of both mechanisms in parallel, with the dominant pathway being strongly dependent of the material system under investigation [22, 27, 28, 47, 52, 53], the initial NP size, [36–38] and specific environmental conditions (annealing temperature, time, surrounding gas/liquid). For a seemingly simple system, the diffusion of Ag islands on Ag single crystal surfaces, different coarsening trends were

observed when either Ag(111) or Ag(100) supports were considered, with Ostwald ripenning being dominant on the former system and diffusion-coalescence on the latter [23]. In general, Ostwald ripening has been reported to underlie sintering phenomena taking place under oxidizing conditions, while diffusion-coalescence has been more commonly observed in reducing environments [25, 28, 47]. For instance, Ostwald ripening was also found to be responsible for the sintering of physical-vapor-deposited (PVD) Ag and Au NPs on TiO_2(110) under CO/O_2 (2:1 ratio, 10 Torr, room temperature) [54]. The latter observation was explained through O_2-induced Au–Au bond weakening. The formation of mobile Au species was also reported for PVD Au NPs on FeO(111) upon exposure to CO/O_2 and CO environments at 1.5 Torr, and assigned to a CO-induced weakening of the NP-support bond [55]. The presence of oxygen vacancies on the support has also been suggested to strongly influence NP mobility and sintering [27, 56–58].

The NP synthesis method and initial NP distribution on the support also strongly influence their stability [24, 25]. Various tactics have been employed in the past to enhance the stability of supported NP catalysts by confining them in mesoporous matrixes, coating them with ligands, partially over-coating the NPs with the support using atomic layer deposition (ALD) methods, as well as through post-preparation chemical redispersion pre-treatments [10, 25, 30, 49, 59–69]. For example, under ultra-high vacuum (UHV) conditions, micelle-synthesized Au and Pt NPs supported on SiO_2/Si(111) and TiO_2(110) were found to be significantly more stable against NP migration and ripening [1, 25, 30, 60, 68–70] than PVD NPs [71, 72]. Nevertheless, following some of these novel synthesis approaches, challenges still remain to ensure that the catalytically active sites remain free from contaminants from the synthesis selected or that the active sites are well accessible to the reactants.

Recently, attention has been paid to monitoring sintering processes not only before and after a given thermal treatment [19–22, 25–29, 73] in a given gaseous or liquid chemical environment, but during the process itself under in situ and *operando* conditions [23, 74–77]. This has been made possible through the development of more sensitive microscopic (i.e. environmental transmission electron microscopy, E-TEM, or high pressure scanning tunneling microscopy, HP-STM) and spectroscopic techniques (i.e. X-ray absorption fine-structure spectroscopy, XAFS, or grazing-incidence small-angle scattering, GISAXS) and their adaptation for use under more realistic conditions (i.e. high temperatures and pressures). For example, sintering due to Ostwald ripening was observed via E-TEM for PVD Pt NPs on thin SiO_2 and Al_2O_3 films under 7.5 Torr of synthetic air (21 % O_2 + 79 % N_2) at 650 °C [50, 51]. In contrast, enhanced stability against sintering and/or redispersion was observed in situ for Pt NPs on nanocrystalline

Al_2O_3 via XAFS when annealed in pure oxygen under atmospheric pressure conditions at 450 °C, or up to 650 °C in H_2 after a pretreatment in pure O_2 [30]. These results highlight that comparisons between seemly analogous material systems can only be made if the thermal treatment is carried out under the same conditions, namely, identical gas content and pressure, temperature, and time. An earlier review article by Bartholomew [78] already warned against the common mistake of generalizing the effect of the environment on NP sintering without considering all experimental details. In particular, annealing highly dispersed (low metal loading) Pt NPs supported on alumina in H_2 at 650 °C results in more sintering as compared to annealing in air [78]. In contrast, the exact same treatment leads to the opposite trend when initially poorly dispersed NPs (high metal loading) are considered.

Therefore, part of the discrepancy found in the literature on the role of O_2 on sintering, with some reports describing enhanced sintering rates under O_2, [47, 50, 51, 79–83] and others describing lack of sintering, NP redispersion and/or loss of material, [30, 73, 84–93] might be simply assigned to the distinct environmental conditions employed. For instance, the partial pressure of oxygen could play a role [82], and the use of synthetic air versus pure O_2 during annealing might favor ripening. In addition, trace amounts of chlorine leftover from metal precursors commonly used in the NP synthesis could also affect the coarsening behavior of the NPs [82, 83, 94]. Finally, another crucial factor influencing the coarsening pathway is the temperature range in which the thermal treatment is performed. Most experiments conducted at temperatures higher than 600 °C in O_2 have revealed significant sintering, [47, 50, 51, 79–81] while treatments at lower temperatures in O_2 showed lower coarsening rates as compared to those in reducing environments [30, 73]. Furthermore, for Al_2O_3-supported Pt NPs, a transition from redispersion to coarsening has been shown to occur in O_2 with increasing temperature [87].

The following review provides some examples of the different factors affecting NP diffusion, coalescence and ripening processes.

2 Experimental

2.1 Sample Preparation

Size-selected Pt and Au NPs with controlled morphologies and uniform dispersion or arrangement were synthesized via inverse micelle encapsulation and deposited on nanocrystalline powder (γ-Al_2O_3, SiO_2, TiO_2, CeO_2) and thin film/single crystal supports [SiO_2(4 nm)/Si(111), TiC/SiO_2(4 nm)/Si(001), and TiO_2(110)] [7, 24, 25, 30, 56, 60,

68, 69]. Their thermal and chemical stability against sintering in O_2, H_2, H_2O, vacuum was studied to unravel how the environment affects the coarsening rate and pathway. Pt/TiO_2 samples prepared via PVD were compared to those prepared by inverse micelle encapsulation in order to study the effect of the synthesis method.

The colloidal NPs were synthesized by dissolving non-polar-polar PS-P2VP diblock copolymers, [poly(styrene)-block-poly(2-vinylpyridine)], in a selective nonpolar solvent (toluene). The polar ends of the block copolymer spontaneously form a cavity with nonpolar ends pointing out into the solvent. Metallic NPs confined in nanoscale cages were obtained by loading these micelles with metal salts ($HAuCl_4$ and H_2PtCl_6), Fig. 1a. This approach allows the self-organized generation of monodispersed NPs with average heights in the range of 0.5–50 nm. The NP size was tuned in two ways: (i) by using polymers with different head sizes (P2VP), and (ii) by changing the metal-salt/polymer core (P2VP) ratio. The distance between NPs can be varied by changing the length of the polymer tail (PS) (e.g. 10–200 nm). Model catalysts consisting of hexagonally-arranged NPs can be obtained after substrate dip-coating into the metal salt-micellar solution, Fig. 1b. Subsequently, the encapsulating polymer can be removed by an in situ O_2/H_2-plasma etch.

In addition to the NP films supported on single crystal substrates, real catalysts (high surface area) were also prepared by adding a nanocrystalline metal oxide support (γ-Al_2O_3, SiO_2, TiO_2, CeO_2) to the liquid NP solution and subsequent solvent evaporation, Fig. 1c. In this case, the organic ligands were removed via prolonged (24 h) annealing treatments in O_2 at 375 °C. O_2 pre-treatments at higher annealing temperatures (500 °C, 2 h) were also conducted for some of these samples to study their coarsening behavior. For both sample types, the removal of the polymer was monitored by measuring the carbon-1s binding energy region via X-ray photoelectron spectroscopy (XPS). This procedure also lead to the removal of Cl from the seed metal salts [31].

Table 1 summarizes the parameters used in the synthesis of the model and real catalysts described above. Relevant morphological information, including the average NP size and interparticle distance is also summarized in Table 2.

2.2 Sample Characterization

Morphological characterization of the model catalyst samples was carried out in air via atomic force microscopy (AFM) (Veeco, Nanoscope III) and in UHV via STM (SPECS GmbH Aarhus-STM). The real catalysts (powders)
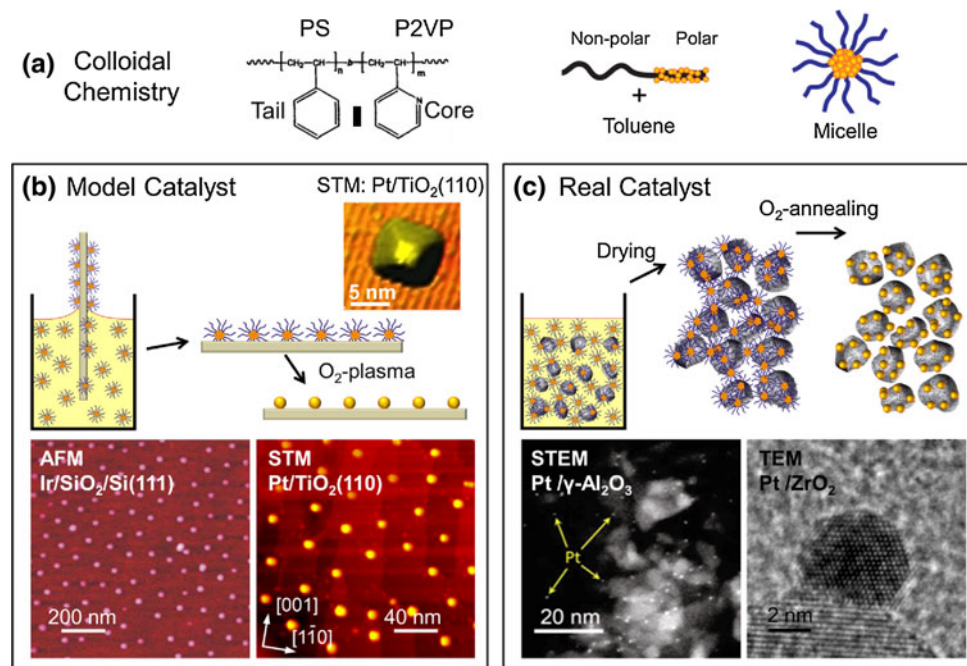

Fig. 1 **a** Schematic of the colloidal chemistry used to synthesize size-selected nanoparticles. **b** Model catalysts: formation of NP films on single crystal substrates and ligand removal via an O_2-plasma treatment. Examples of typical NP and sample morphologies corresponding to Ir and Pt NPs deposited on $SiO_2/Si(111)$ and $TiO_2(110)$ acquired via AFM (*bottom left* [60]) and STM (*top* [106] and *bottom right* [69]) are shown. **c** real catalysts: impregnation of the

micellar NP solution on high surface area nanocrystalline supports and polymer removal by annealing in oxygen. Examples of typical NP and sample morphologies corresponding to Pt NPs supported on nanocrystalline γ-Al_2O_3 and ZrO_2 acquired via HAADF-STEM (*bottom left* [130]) and conventional TEM (*bottom right* [31]) are shown

were investigated via high-angle annular dark field (HA-ADF) scanning transmission electron microscopy (STEM). A suspension created by mixing the powder samples with ethanol was placed on a carbon-coated TEM Cu grid. HAADF images were acquired with a JEOL 2010F TEM operated at 200 kV and a Tecnai F30 TEM operated at 300 kV. The probe size of STEM is about 0.14 nm.

Extended X-ray absorption fine-structure (EXAFS) spectroscopy measurements were acquired at beamlines 18B and 19A at the National Synchrotron Light Source at Brookhaven National Laboratory (NSLS-BNL) in transmission and fluorescence modes. The powder samples were pressed into thin pellets and placed either inside a quartz tube surrounded by a clam-shell furnace or inside a reactor cell with heating and cooling capabilities. The Athena and Artemis programs from the Ifeffit software package were used to process and analyze the EXAFS data acquired [95–97]. Theoretical EXAFS signals were constructed with the FEFF6 program [98] using the model structure of face-centered-cubic (fcc) Pt.

The catalysts were also characterized via monochromatic XPS (Al $K\alpha = 1,486.6$ eV) at the University of Central Florida and via high pressure XPS at Lawrence Berkeley National Laboratory ($E_{h\upsilon} = 490$ eV).

3 Results and Discussion

3.1 Influence of the Nanoparticle Synthesis Method on Sintering

In order to obtain a more in depth view of the thermal stability of NPs, a thorough understanding of the different pathways underlying thermally-driven coarsening phenomena, and the effect of the NP synthesis method, support morphology, and degree of support reduction on NP sintering is needed. In the following study [25], the sintering of $TiO_2(110)$-supported Pt NPs synthesized either via PVD or inverse micelle encapsulation, was monitored via STM in UHV, Fig. 2. The experimental investigation was accompanied by simulations following the Ostwald ripening and diffusion-coalescence models, Fig. 3.

3.1.1 Physical-Vapor-Deposited Nanoparticles (UHV Anneal)

Figure 2 shows STM images from two samples prepared with a similar amount of Pt evaporated on pristine $TiO_2(110)$ (S1), Fig. 2a, b, and a $TiO_2(110)$ substrate which was coated with the same polymer used for the micellar sample preparation (see next section) prior to Pt

evaporation (S2), Fig. 2d, e. The polymer-coated sample (S2) was cleaned using an O_2 plasma treatment, leading to complete NP oxidation, and then both samples were annealed stepwise from RT up to 1,060 °C. The images shown were acquired at room temperature after annealing at 930 °C (Fig. 2a, d) and 1,060 °C (Fig. 2b, e).

Larger NPs with lower NP surface density were observed on the polymer-coated TiO_2 substrate (S2), Fig. 2f indicating the higher rate of coarsening as compared to the NPs supported on pristine reduced TiO_2, Fig. 2c. This finding demonstrates that any leftover polymeric layer which might remain underneath the NPs in S2 after the pre-treatment in O_2 does not act as interfacial "glue" to stabilize the NPs against sintering.

To better understand the coarsening behavior of the PVD NPs, simulations were carried out following two different coarsening models: Ostwald ripening and diffusion-coalescence. A detailed description of the physical parameters accounted for in both models is given in Ref. [25]. Here, we have to mention that the simulation models do not represent all the complexities of the real sample and therefore, these theoretical results do not perfectly follow the experimental data. Nevertheless, for both samples (S1, S2), the best agreement between the simulation results and the experimental data was obtained for the diffusion-coalescence pathway, Fig. 3. In contrast, following the Ostwald-ripening model the simulated NP size distribution was found to be always narrower than that obtained experimentally, suggesting that the dominant coarsening pathway for both samples in vacuum is the diffusion-coalescence route.

3.1.2 Colloidal Nanoparticles: Inverse Micelle Encapsulation Synthesis (UHV Anneal)

In order to explore the role of the initial NP geometry and sample morphology (NP size and interparticle distance) on their thermal stability, model NP catalysts consisting of size-selected colloidal NPs synthesized via inverse micelle encapsulation were studied [25, 69]. Before annealing, this sample (S3) was exposed to an O_2-plasma treatment to remove the polymeric ligands followed by a stepwise thermal treatment in UHV up to 1,060 °C. Nevertheless, contrary to the analogously-treated PVD-NPs in S2, enhanced thermal stability was observed for the micellar Pt NPs, not showing any significant sintering at 1,060 °C, Fig. 2g, h. The latter might be related to the initial narrower NP size distribution in the micellar sample (S3), lower NP density on the support surface with large ∼30 nm and regular interparticle distances, and a stronger NP/support interface. The role of the initial interparticle distance in coarsening phenomena is illustrated in more detail in the next section.

Table 1 Parameters used in the synthesis of Pt and Au NPs via inverse micelle encapsulation and PVD. Information on the NP size (height and/or diameter) extracted from AFM, STM, and TEM measurements are also shown

Sample/characterization method	Synthesis	Treatment and characterization: NP height (h), diameter (d), interparticle distance (IP), all in nm	Conclusion
(a) Synthesis method			
S1, Pt/TiO$_2$(110) STM	PVD Model catalyst	Annealing in UHV 930 °C (h = 0.5 ± 0.2, IP = 7 ± 3)→ 1,060 °C (h = 1.0 ± 0.3, IP = 12 ± 5)	Figure 2a–c: coarsening through diffusion–coalescence.
S2, Pt/polymer/TiO$_2$(110) STM	PVD Model catalyst	O$_2$-plasma treatment → annealing in UHV 930 °C (h = 0.8 ± 0.3, IP = 9 ± 4)→ 1,060 °C (h = 1.3 ± 0.6, IP = 13 ± 7)	Figure 2d–f: more coarsening than S1 also through diffusion-coalescence.
S3, Pt/TiO$_2$(110) STM	Micelle Model catalyst	O$_2$-plasma treatment → annealing in UHV 500 °C, 1,000 °C (h = 3.1 ± 0.6, IP = 28 ± 5)→ 1,060 °C (h = 3.0 ± 0.9, IP = 30 ± 7)	Figure 2g–i: lack of coarsening.
(b) Interparticle distance			
S4, Au/TiC/SiO$_2$/Si(111) AFM	Micelle Model catalyst	Annealing in UHV at 500 °C Initial (h = 2.1 ± 0.4, IP = 27 ± 6), 5 CO Oxidation TPD cycles (227 °C)	Figure 4a, b: drastic coarsening, loss of initial hexagonal NP arrangement.
S5, Au/TiC/SiO$_2$/Si(111) AFM	Micelle Model catalyst	Annealing in UHV at 500 °C Initial (h = 1.9 ± 0.5, IP = 78 ± 12), 17 CO Oxidation TPD cycles (227 °C)	Figure 4c, d: similar size but larger interparticle distance as compared to S4 → lack of coarsening.
S6, Au/TiC/SiO$_2$/Si(111) AFM	Micelle Model catalyst	Annealing in UHV at 500 °C Initial (h = 6.1 ± 1.0, IP = 44 ± 9) → 5 CO oxidation TPD cycles (bimodal h = 2.2 ± 0.6 and 8.3 ± 1.7)	Figure 4e, f: coarsening resulting in bimodal NP size distribution.
S7, Au/TiC/SiO$_2$/Si(111) AFM	Micelle Model catalyst	Annealing in UHV at 500 °C Initial (h = 3.6 ± 0.8, IP = 76 ± 9)→ 5 CO oxidation TPD cycles (h = 3.6 ± 0.8)	Figure 4g, h: larger average IP distance as compared to S6 → lack of coarsening.
(c) Support effect			
S8, Pt/Al$_2$O$_3$ (2 wt%) TEM	Micelle Real catalyst	Annealing in O$_2$ for 24 h at 500 °C (d = 8.7 ± 2.1)	Figure 5: larger NPs due to coarsening on CeO$_2$ and SiO$_2$ and smaller NPs on Al$_2$O$_3$ and ZrO$_2$. The effect of NP-support interaction and also the specific surface area of the support was studied. Lower coarsening rates were obtained on the substrates with the highest surface areas.
S9, Pt/ZrO$_2$ (2 wt%) TEM	Micelle Real catalyst	Annealing in O$_2$ for 24 h at 500 °C (d = 8.3 ± 1.6)	
S10, Pt/CeO$_2$ (2 wt %) STEM	Micelle Real catalyst	Annealing in O$_2$ for 24 h at 500 °C (d = 14.6 ± 2.7)	
S11, Pt/SiO$_2$ (2wt %) TEM	Micelle Real catalyst	Annealing in O$_2$ for 24 h at 500 °C (d = 15 ± 10)	

Table 1 continued

Sample/characterization method	Synthesis	Treatment and characterization: NP height (h), diameter (d), interparticle distance (IP), all in nm	Conclusion
S12, Pt/TiO$_2$/SiO$_2$/Si(001) AFM	Micelle Model catalyst	RT O$_2$-plasma treatment, Initial (h = 3.3 ± 0.6, IP = 30)→ Annealing in UHV to 727 °C	Figure 6: UHV annealing resulted in total burial of Pt NPs in polycrystalline TiO$_2$ while no significant morphological change took place on Pt/SiO$_2$. Similar micellar Pt NPs (S3) did not become embedded in single crystal TiO$_2$(110).
S13, Pt/SiO$_2$/Si(001) AFM	Micelle Model catalyst	RT O$_2$-plasma treatment Initial (h = 2.6 ± 0.4, IP = 30)→ Annealing in UHV up to 727 °C (h = 1.5 ± 0.2)	
(c) Pre-treatment effect			
S14, Pt/γ-Al$_2$O$_3$ (1 wt%) HAADF-STEM, EXAFS	Micelle Real catalyst	Ex situ: annealing in O$_2$ at 200 °C Initial (d = 0.3 ± 0.1), in situ: O$_2$ at 400 → in situ: H$_2$ 400–800 °C (d = 1.0 ± 0.2)	Figure 7: pre-treatment in oxygen resulted in higher stability of Pt NPs against subsequent coarsening in H$_2$ up to 800 °C (S14) as compared to a similar sample only exposed to H$_2$ (S15).
S15, Pt/γ-Al$_2$O$_3$ (1 wt%) HAADF-STEM, EXAFS	Micelle Real catalyst	Initial (d = 0.3 ± 0.1), In situ: annealing in H$_2$ at 400 °C → In situ: H$_2$ 400–800 °C (d = 5.0 ± 1.5)	
(d) Environment effect			
S16, Pt/γ-Al$_2$O$_3$ (1 wt%) HAADF-STEM, EXAFS	Micelle Real catalyst	Ex situ: annealing in O$_2$ at 375 °C, In situ: H$_2$ at 375°, initial (d = 0.5 ± 0.1)→ In situ: O$_2$ at 450 °C (d = 0.6 ± 0.2)	Figure 8: similarly prepared samples annealed for 3 h at 450 °C were found to coarsen the most in a H$_2$ environment and the least under O$_2$. The coarsening in H$_2$O vapor is somewhat in between that of H$_2$ and O$_2$. Possible stabilizing role of PtO$_x$ species at the NP/support interface.
S17, Pt/γ-Al$_2$O$_3$ (1 wt%) HAADF-STEM, EXAFS	Micelle Real catalyst	Ex situ: annealing in O$_2$ at 375 °C In situ: H$_2$ at 375°, initial (d = 0.5 ± 0.1)→ In situ: H$_2$O at 450 °C (d = 0.8 ± 0.3)	
S18, Pt/γ-Al$_2$O$_3$ (1 wt %) HAADF-STEM, EXAFS	Micelle Real catalyst	Ex situ: annealing in O$_2$ at 375 °C In situ: H$_2$ at 375°, initial (d = 0.5 ± 0.1)→ In situ: H$_2$ at 450 °C (d = 1.2 ± 0.3)	
S19, Pt/SiO$_2$/Si(111) AFM, HP XPS	Micelle Model catalyst	O$_2$-plasma treatment, initial (h = 2.0 ± 0.5) In situ annealing in H$_2$ and O$_2$ at 100–600 °C, (h = 1.3 ± 0.4)	Figure 9: material loss during heat treatment in O$_2$ due to volatile Pt oxide formation and their possible quick removal via differential pumping.

3.2 Influence of the Interparticle Distance on Sintering

The coarsening rate of supported NPs through the diffusion-coalescence pathway is proportional to the NP density on the support surface [25]. Furthermore, there are two different rate-limiting regimes for the Ostwald-ripening coarsening pathway: (i) interface-controlled, in which the rate limiting step is detachment/attachment of individual atoms from/to the NPs, and (ii) diffusion-controlled, in which the rate limiting step is the diffusion of atoms from one NP to another. In the former case, the NP density has no effect on the coarsening rate, while in the latter an increase in the interparticle distance would also lead to a decrease in the coarsening rate [22, 25, 42, 43, 99].

In addition to the standard models of diffusion-coalescence in which the diffusion of the NPs on the surface is completely random, it has been suggested that a directed diffusion could also occur due to a non-uniform adatom concentration on the support when two NPs are sufficiently close [100, 101]. Thus, increasing the interparticle distance could reduce the coarsening rate through most of the coarsening pathways, namely, the diffusion-coalescence route, the diffusion-limited Ostwald ripening, as well as the coalescence pathway via directed NP motion.

In order to gain insight into the effect of the NP distribution on the support surface on coarsening, two samples containing Au NPs with similar average heights (∼2 nm), but with different average interparticle distances (∼30 nm
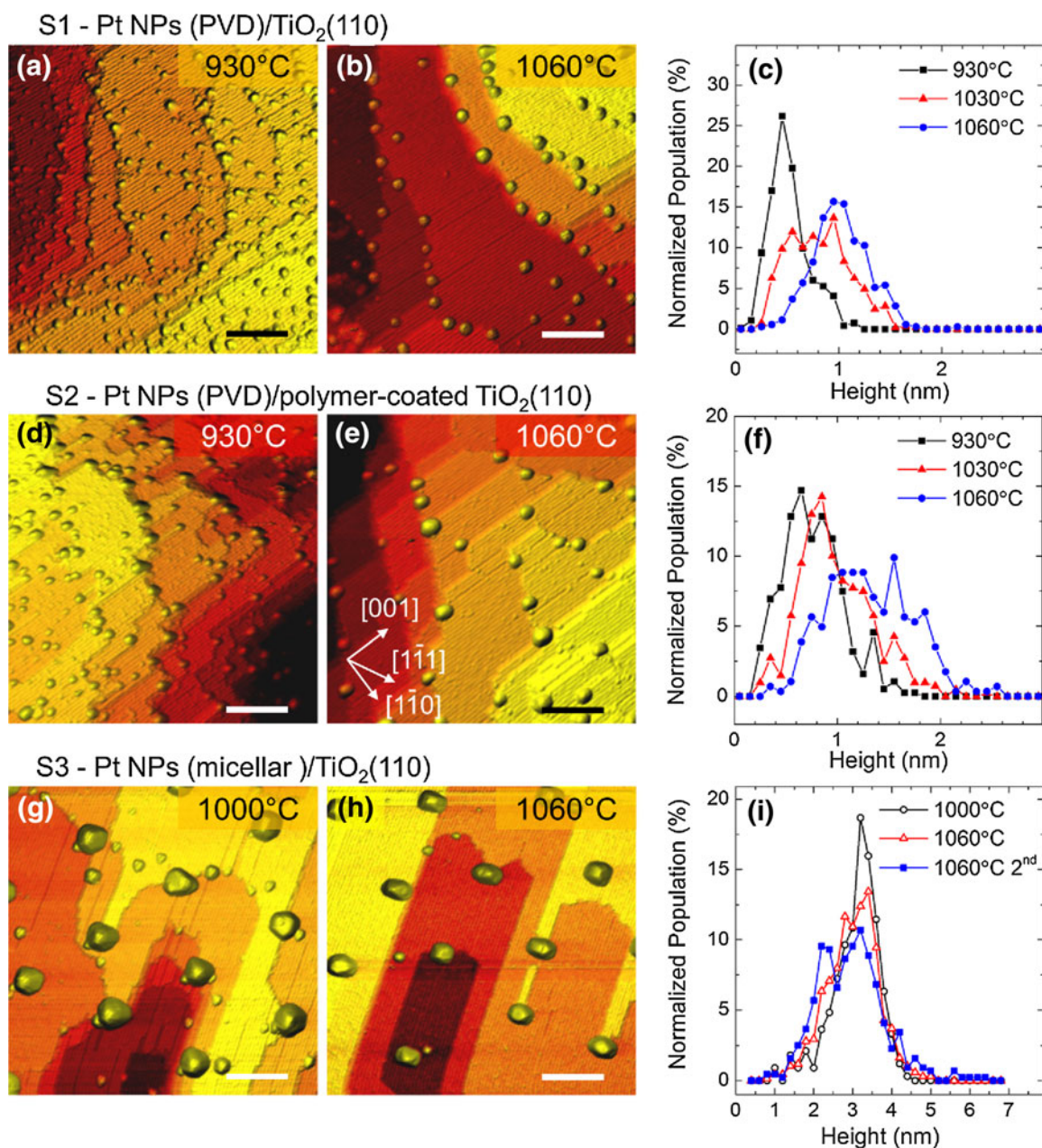
Fig. 2 STM images of **a, b** PVD Pt NPs/pristine-TiO$_2$(110) (S1), **d, e** PVD Pt NPs/polymer-coated TiO$_2$(110) (S2), **g–i** micelle-synthesized Pt NPs/TiO$_2$(110) (S3). All images were acquired in UHV at RT after in situ sample annealing at 930 °C (**a, d**), 1,000 °C (**g**) and at 1,060 °C (**b, e, h**) [25]. The *scale bar* in all images is 20 nm. Nanoparticle height (**c, f, i**) extracted from the analysis of STM images obtained at RT after annealing in UHV [25]

for S4 and ∼80 nm for S5), were synthesized using di-block copolymer encapsulation and deposited on thin TiC films [24]. Figure 4 shows AFM images of these samples acquired after ligand removal by annealing at 500 °C in UHV (a) S4 and (c) S5. Subsequently, the samples were exposed to CO + O$_2$ (0.6 + 0.3 L) at low temperature (∼95 K) and their chemical reactivity for the oxidation of CO investigated by successive temperature programmed desorption (TPD) cycles, Fig. 4b, d. Surprisingly, reactive

coarsening and subsequent deactivation was only observed for the sample with the smaller initial interparticle distance (S4). Instead, the system with the larger average interparticle distance (S5) showed higher stability against agglomeration, no loss of active surface area, and longer lifetime.

A similar trend was also observed for larger NPs ∼6.1 nm in S6 and ∼3.6 nm in S7, where the non-uniformly and closely-spaced NPs in S6 (average interparticle
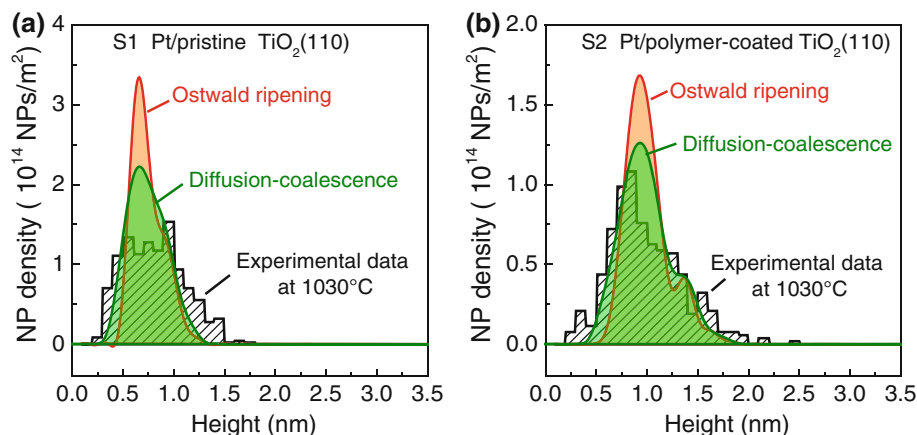
Fig. 3 Comparison between the Ostwald ripening and diffusion-coalescence simulation results and the experimental size distribution of samples S1 and S2 after annealing in UHV at 1,030 °C. The simulations were conducted using the experimental size distributions obtained via STM before the 1,030 °C as the initial size distributions and following the same thermal treatment applied to samples S1 and S2 [25]. The Ostwald ripening simulation leads to a narrower size distribution as compared to the experimental data. A better agreement is obtained following the diffusion-coalescence model

distance of 44 nm) were found to be prone to reactant-mediated ($CO+O_2$) Ostwald ripening, Fig. 4f, leading to a final bimodal size distribution (maxima at 2.2 and 8.3 nm). In contrast, the more widely spaced (76 nm) NPs in S7 retained their initial size after a similar treatment, Fig. 4h. It should be mentioned that the small features seen between the micellar NPs in Fig. 4a ,b are not small Au NPs, but correspond to the pearl-like structure of the $TiC/SiO_2/Si(111)$ support obtained after the pre-treatment in UHV. Unlike PVD prepared samples, there are no small NPs (e.g. monomers, dimers, etc.) in between the micellar NPs. Furthermore, in these samples NP features can be distinguished from substrate roughness (or small clusters/impurities) based on the nearly hexagonal arrangement displayed by the metal NPs. The slight difference in NP density observed when comparing the images in Fig. 4g, h is due to the drift of the AFM scanner resulting in an expansion of the image in Fig. 4h.

In addition, size-dependent Ostwald ripening has been previously reported during CO oxidation for PVD Au NPs on $TiO_2(110)$ [54]. Therefore, the differences in the initial average NP sizes in both samples must be considered in the latter example. Interestingly, the larger NPs in S6 should be more stable against coarsening as compared to the smaller NPs in S7. In this case, the effect of interparticle distance seems to be dominating the coarsening behavior rather than the size effect.

Although Ostwald ripening was shown to be the main coarsening pathway for PVD-prepared $Au/TiO_2(110)$ during CO oxidation at low temperature (RT to 137 °C) [102], coarsening through diffusion-coalescence cannot be ruled out in our case due to the slightly higher treatment temperature (227 °C) and different support (TiC vs TiO_2 in Ref. 102). Our indirect study does not allow us to separate

both sintering pathways. In addition, it has been shown that in some cases both coarsening routes may coexist [100, 103], and that the dominant coarsening pathway may vary with increasing temperature [104, 105].

The above findings illustrate the crucial role that the rational design of a nanocatalyst, i.e. the selection of its initial size, size distribution and dispersion on a surface may have in its performance, stability, and durability.

3.3 Support Effects

The sintering or redispersion behavior of NPs can be affected by a variety of support properties, such as metal-support interaction and adhesion energy, support surface area, surface trap sites, and support reducibility. For example, a strong NP-support interaction would decrease the coarsening rate through the diffusion-coalescence pathway. However, a stronger interaction could increase the probability of sintering via a Ostwald ripening process in cases where the rate limiting step is the metal atom detachment from the NPs. Surface trap sites such as vacancies and step edges could also stabilize the NPs, favoring the growth of trapped NPs at the expense of the disappearance of those located at regular surface sites. Such phenomenon could occur through both, Ostwald ripening and diffusion-coalescence.

In order to study the support effect on the coarsening behavior of inverse micelle prepared Pt NPs, four samples (S8–S11) [56] were prepared with an identical micellar solution but impregnated on different high surface area powder supports, namely, Al_2O_3 (S8), ZrO_2 (S9), CeO_2 (S10), and SiO_2 (S11) (Fig. 5). Subsequently, the samples were annealed in air at 500 °C for 2.5 h. The NPs supported on Al_2O_3 and ZrO_2 were found to have an average

Fig. 4 AFM images of micelle-synthesized Au NPs supported on TiC films (**a**, **b**) S4 [24], (**c**, **d**) S5 [24], (**e**, **f**) S6 [7], (**g**, **h**) S7 [7] acquired ex situ at room temperature. Images (**a**, **c**, **e**, **g**) were recorded after annealing in UHV at 500 °C, and (**b**, **d**, **f**, **h**) after CO oxidation (5 TPD cycles for S4, S6, and S7, and 17 cycles for S5)
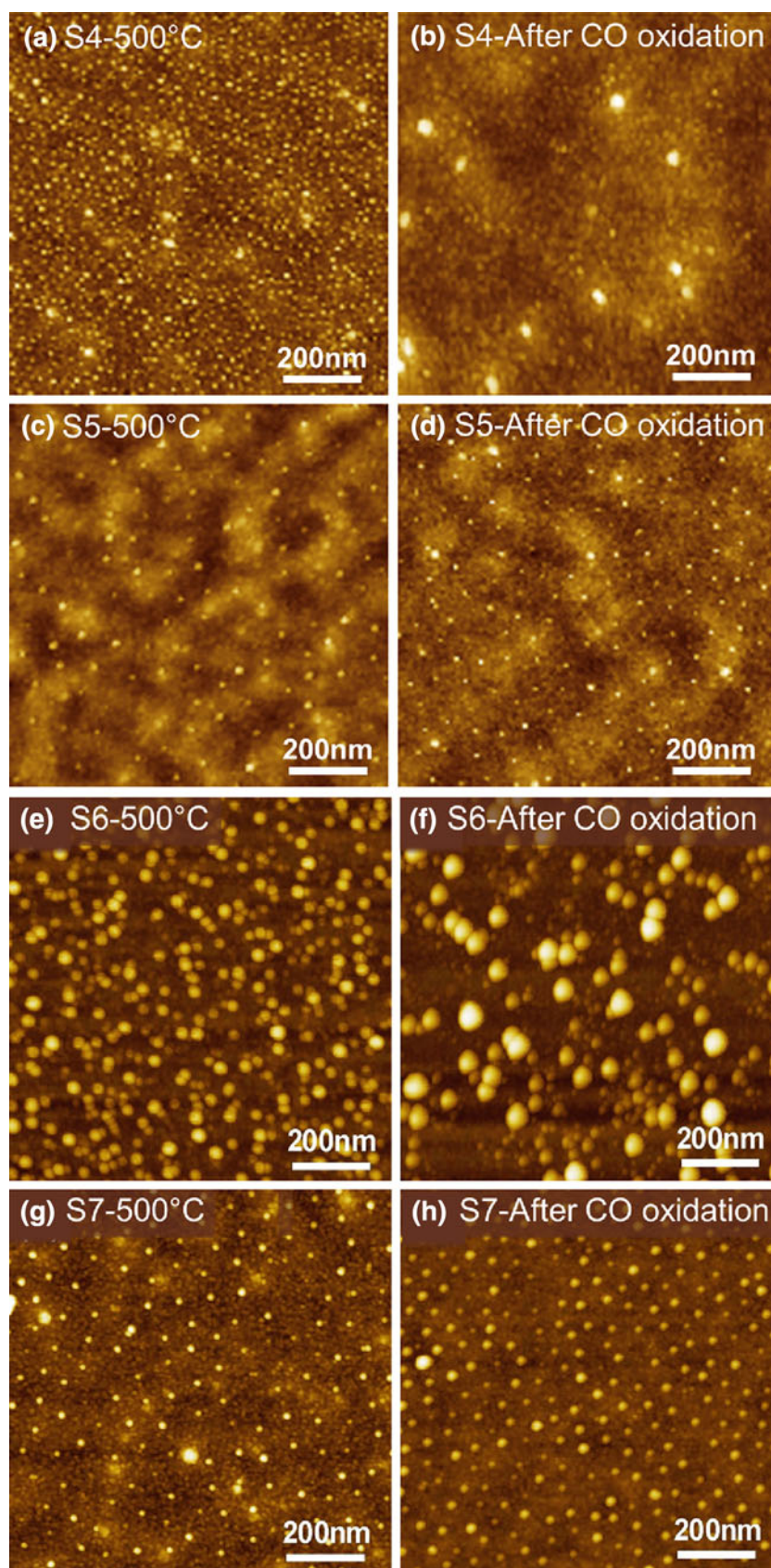
size of ~ 8.5 nm, while those supported on CeO_2, and SiO_2 were found to be coarsened, with an average size of ~ 15 nm. Such drastic difference in NP size could be understood in terms of the support effect, since all samples were prepared using an identical micelle solution and were subjected to a similar thermal treatment. In the case of the SiO_2-supported NPs the main factor resulting in higher coarsening rate is the lower surface area of the SiO_2 support as compared to other samples studied here. A lower support surface area results in higher NP surface density and therefore increases the coarsening rate as was shown in the previous section for model catalysts (samples S4–S7). On the other hand, the chemical composition, stoichiometry, and density of defects in the support must also be considered. The nature of the metal NP-support interaction is more complex for reducible supports such as CeO_2 and TiO_2 which are known to change dramatically upon annealing in reducing environments and to show strong metal-support interactions (SMSI). Such strong interactions could result in NP encapsulation by a thin layer of the support in case of TiO_2, or atomic diffusion of metal atoms into the support and alloy formation in case of CeO_2.

As was mentioned before, the metal salt to PV2P ratio determines the final size of the micelle-synthesized NPs. Larger Pt NPs on γ-Al2O3 were initially obtained in S8 as compared to S16-S18 due to the use of a higher metal/ P2VP ratio (0.6 vs for S8 vs 0.05 for S16–18). In addition, a higher metal/support weight ratio was used (2 % for S8 and 1 % for S16–18). Furthermore, before the coarsening study, both type of samples were treated differently. In particular, S8 was annealed in air at 500 °C for 24 h before any ligand removal, while S16 was annealed in pure oxygen at 450 °C for 4 h only after the removal of the polymeric ligands (pre-treatment in O_2 at 375 °C for 24 h). Our studies indicate that micellar NPs are more susceptible to
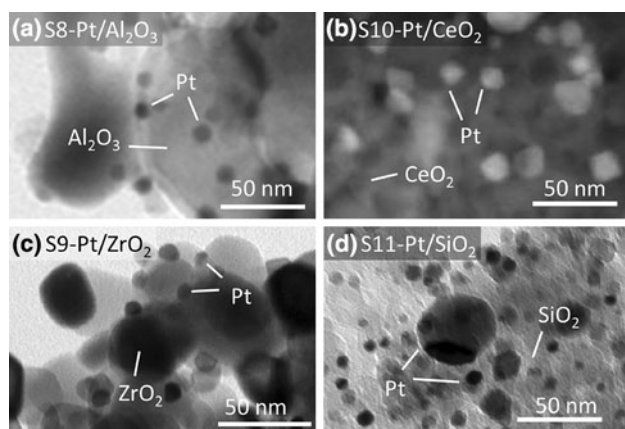
coarsening during the polymer removal annealing since the NP/support adhesion is not established yet. In fact, a thermal treatment that may cause NP coarsening for micellar NPs encapsulated by the polymeric ligands, may not result in sintering of analogous but ligand-free NPs. Therefore, when using colloidal methods for the synthesis of NP catalysts, special care should be taken in choosing the proper temperature, annealing environment and time for polymer removal treatment to avoid unwanted NP coarsening.

To further investigate the support effect, samples S12 and S13 were prepared using identical micellar solutions but on different supports [70]. Sample S12 was supported on TiO_2(7 nm)/Ti(6 nm), and S13 on SiO_2(4 nm)/Si(001). After subsequent in situ isochronal annealing from 70 °C to 727 °C in UHV, no significant changes were observed for S13 supported on SiO_2, Fig. 6c. However, for S12 the same thermal treatment resulted in reduction of the TiO_2 layer into TiO_x and the complete encapsulation of the Pt NPs inside the TiO_x layer, Fig. 6a, b. Interestingly, such complete submersion of Pt NPs in TiO_2 was not observed for identical micellar NPs supported on single crystal TiO_2(110) (sample S3), even after annealing at higher
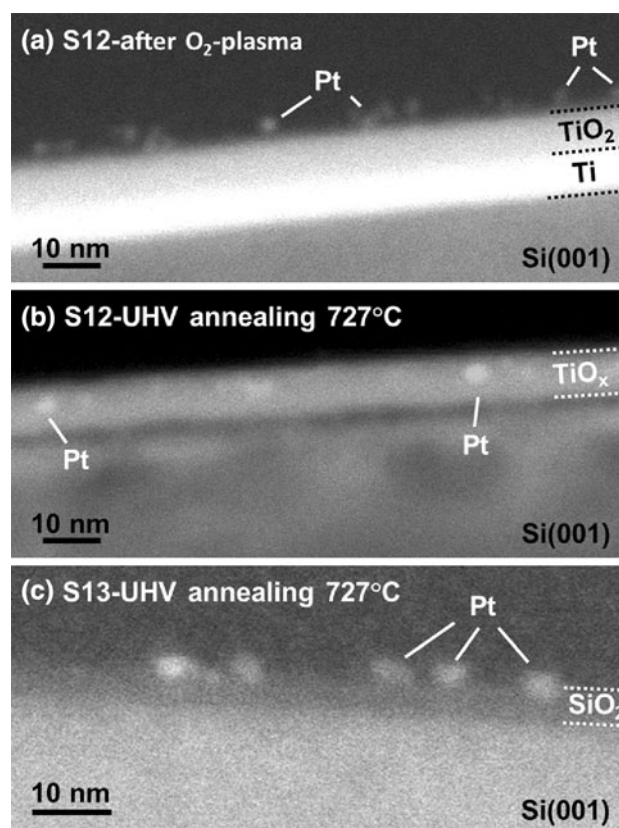

Fig. 6 Cross sectional STEM images of Pt NPs supported on **a**, **b** TiO_2 (7 nm)/Ti(8 nm)/Si(001) and **c** SiO_2(4 nm)/Si(001), after **a** O_2-plasma exposure at RT and **b**, **c** after subsequent in situ isochronal annealing from 70 to 727 °C in UHV [70]

Fig. 5 TEM (**a**, **b**, **d**) and STEM (**c**) images of inverse micelle prepared Pt NPs supported on **a** Al_2O_3, **b** ZrO_2, **c** CeO_2 and **d** SiO_2 after O_2 treatment at 500 °C for 2.5 h

temperature (1,060 °C), Fig. 2h. This example highlights the complexity of the support effect and shows that not only the support material but also its crystalline structure, reduction degree and thickness should be taken into account.

3.4 Pre-treatment Effects

Distinct activities/selectivities have been reported for NP catalysts exposed to different chemical/thermal pre-treatments [25, 30, 31, 49, 80]. Nevertheless, although the importance of such catalyst activation pre-treatments is widely recognized in multiple industrial applications, the origin of the distinct catalytic performance observed is in many cases not well understood. For example, a given pre-treatment might influence the initial chemical state of the catalysts [30], might lead to distinct NP geometries (changes in NP size and shape) [25], to the removal of residual byproducts from the synthesis process [47], to modified NP/support interfaces (different structures, different contact areas, or to the presence of adsorbed/intercalated chemical species at the NP/support interface) [106], and to NP redispersion [82], or sintering [82].

In this study, the thermal stability of size-selected micelle-synthesized Pt NPs supported on nanocrystalline γ-Al₂O₃ was investigated in situ after different pretreatments via EXAFS and ex situ via HAADF-STEM [30]. The details regarding sample preparation parameters can be found in Table 1. Significant differences in the thermal stability of identically prepared Pt/γ-Al₂O₃ samples (S14 and S15) exposed to two different pre-treatments were observed, Fig. 7. In particular, exposure to O₂ at 375 °C (S14) before high temperature annealing in H₂ (800 °C) was found to result in the stabilization of the micellar Pt NPs, reaching a maximum overall size after coarsening in H₂ at 800 °C of ∼1 nm, Fig. 7b. Interestingly, when an analogous sample (identical micellar solution) (S15) was pre-treated in H₂ at ∼400 °C, a final size of ∼5 nm was reached when subsequently annealed in hydrogen at 800 °C, Fig. 7d. These ex situ data demonstrate the importance of the pre-treatment step in the following stability of nanosized catalysts.

Additional in situ work was conducted on this system, specifically, on the most stable sample, S14, in order to gain insight into the onset temperature for sintering under hydrogen (at atmospheric pressure). Figure 7e shows Fourier transform EXAFS spectra of S14 acquired in situ at various temperatures in H₂, together with the oxidized state of the as-prepared sample (He data). Annealing in O₂ at 375 °C leads to the formation of PtOₓ species, as demonstrated by the low-r Pt–O component at ∼1.6 Å (phase uncorrected). Subsequent in situ annealing at 400 °C in H₂ leads to the disappearance of the former feature and

complete reduction of the Pt NPs. After NP reduction, a decrease in the overall intensity of the Pt–Pt EXAFS signal with increasing measurement temperature up to 650 °C is observed, which is consistent with the effect of thermal bond length disorder. Systematic differences were observed among individual scans acquired at 800 °C and therefore, three representative scans acquired at 800 °C are shown in Fig. 7e. The sudden increase in the magnitude of the Fourier transform main Pt–Pt component observed at 800 °C as compared to the 650 °C data can only be explained if the growth (coarsening) of the NPs is considered. In the latter case, the increase in the 1st nearest neighbor (NN) coordination number (CN) will compensate the decrease in the signal induced by thermal disorder. At the same time, the static disorder (EXAFS Debye–Waller factor extrapolated to 0 K) is expected to decrease due to the larger fraction of interior, bulk-like bonds within the larger NPs, which also leads to an increase in the EXAFS signal. From the fit of the EXAFS spectra in Fig. 7e, the Pt–Pt distances and 1st NN CNs (NN1) were obtained at different temperatures, Fig. 7f. The average NP sizes at different temperatures were extracted from the 1st NN CNs using a large database of a variety of fcc Pt NP shapes with different sizes, Fig. 7g [30]. Figure 7f, g demonstrate lack of sintering for S14 in H₂ up to at least 650 °C, with an increase in the average NP size only observed upon further heating to 800 °C. Nevertheless, the final average NP size obtained for S14 (∼1.8 nm according to the EXAFS data and ∼1.0 nm according to TEM) at 800 °C was significantly smaller than that of the H₂-pretreated sample (S15) at much lower temperature. In fact, even at 400 °C in H₂ (i.e. directly after the pre-treatment), a 1st NN coordination number of 9.3 was obtained for S15 (H₂-pretreated), and only 6.9 for S14 (O₂-pretreated).

3.5 Environmental Effects (H₂, O₂, H₂O)

The beneficial role of oxygen for the stabilization of small Pt NPs was also observed ex situ via HAADF-STEM and in situ via EXAFS during annealing treatments in O₂ at 450 °C for three hours at atmospheric pressure, Fig. 8 [30]. In particular, while NPs of 0.5 ± 0.1 nm initial average size did not display any significant sintering in oxygen (0.6 ± 0.2 nm final size, S16), an analogous thermal treatment of an identical sample in hydrogen (S18) lead to NP coarsening (1.2 ± 0.3 nm), Fig. 8b, d, respectively. The same sample type pre-dosed and annealed in an atmosphere containing water vapor only displayed moderate sintering (0.8 ± 0.3 nm) (S17), Fig. 6c. Since STEM is a local probe allowing sampling of relatively small sample regions, our microscopic observations were compared to ensemble-averaging data extracted from EXAFS measurements.

Fig. 7 a–d HAADF-STEM images of Pt NPs supported on γ-Al₂O₃ prepared using an identical micellar NP solution acquired (**a**, **c**) as-prepared, and (**b**, **d**) after sequential annealing in hydrogen from 400 to 800 °C. Images (**a**, **b**) correspond to S14 [30] and (**c**, **d**) to S15 [30]. These samples differ in the pre-treatment (as-prepared state). Sample S14 was pre-treated in O₂ at 200 °C (**a**), while S8 was only dried in air at 60 °C (**c**). Subsequently, S14 was annealed in O₂ at 375 °C followed by H₂ from 400 to 800 °C, while S15 was only exposed to hydrogen at the same temperatures. **e** Fourier transform EXAFS data obtained for S14 in situ during treatments in O₂ (375 °C) and H₂ (400–800 °C, total annealing time ∼6 h). **f** Evolution of the 1st NN coordination number (NN1) and **g** EXAFS-estimated NP size of S14 during the different annealing treatments. For reference, the initial NN1 and NP size of S15 after the different pretreatment are also shown
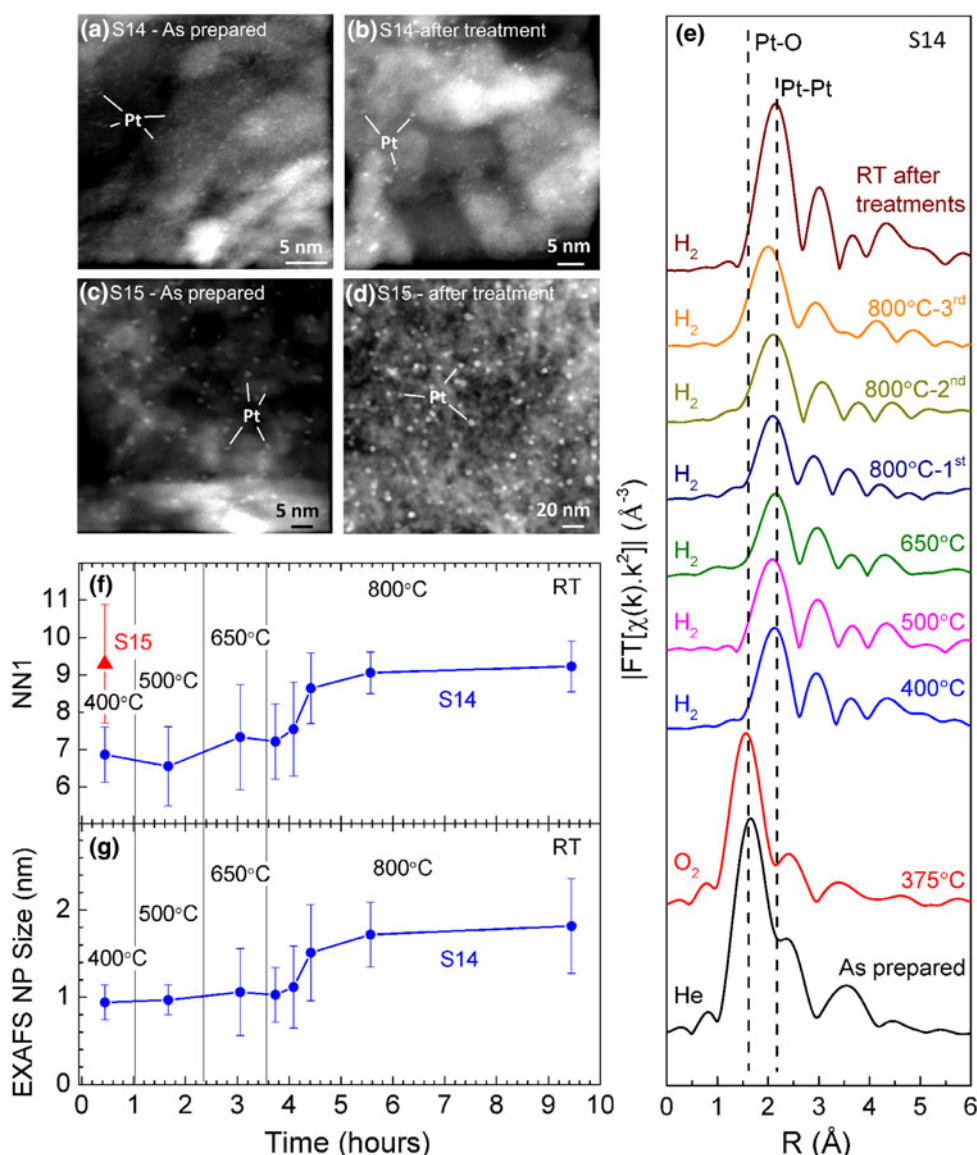
Fourier transform EXAFS data (r-space) acquired at 450 °C in the different environments revealed the presence of a large Pt–O component from PtO_x species under O₂, no Pt–O component under H₂, and both, Pt–O and Pt–Pt contributions under H₂O, Fig. 8e. Subsequently, all three samples were reduced in H₂ at 375 °C and EXAFS measurements acquired in H₂ at RT, Fig. 8f. Interestingly, the lowest average 1st NN coordination number was obtained for the sample previously exposed to O₂ (6.9 ± 0.4), and the largest NN1 for that heated in H₂ at 450 °C (8.3 ± 0.4), with the sample exposed to H₂O being in between (7.3 ± 0.3). A schematic model of our experimental observations is shown in Fig. 8g.

Since the samples displaying Pt–O bonds were the most stable against sintering (O₂ and H₂O-vapor annealed), our data suggest that PtO_x species, possibly modifying the NP/support interface, play a role in the stabilization of small Pt

NPs. An enhanced thermal stability of O₂-annealed samples (400–500 °C) was also previously observed for Pt NPs/Al₂O₃ [73, 107–110], and Au NPs/SiO₂ [19]. The stabilizing role of PdO_x species was also discussed by Goeke and Datye [49] for Pd NPs synthesized by electron beam evaporation based on the comparison of SEM data acquired after annealing in O₂ at 700 °C versus an identical treatment in an inert atmosphere (N₂). The former data are in agreement with our observations, where sample annealing in reducing environments (e.g. hydrogen) leads to PtO_x reduction, the consequent weakening of the NP/support bond, and NP sintering [84, 85, 111].

Although further work is still needed in order to clarify the origin of the enhanced thermal stability of samples pre-treated in O₂ at moderate temperatures (375–450 °C, samples S14 and S16), an initial O₂-mediated NP redispersion might contribute to this effect. Redispersion
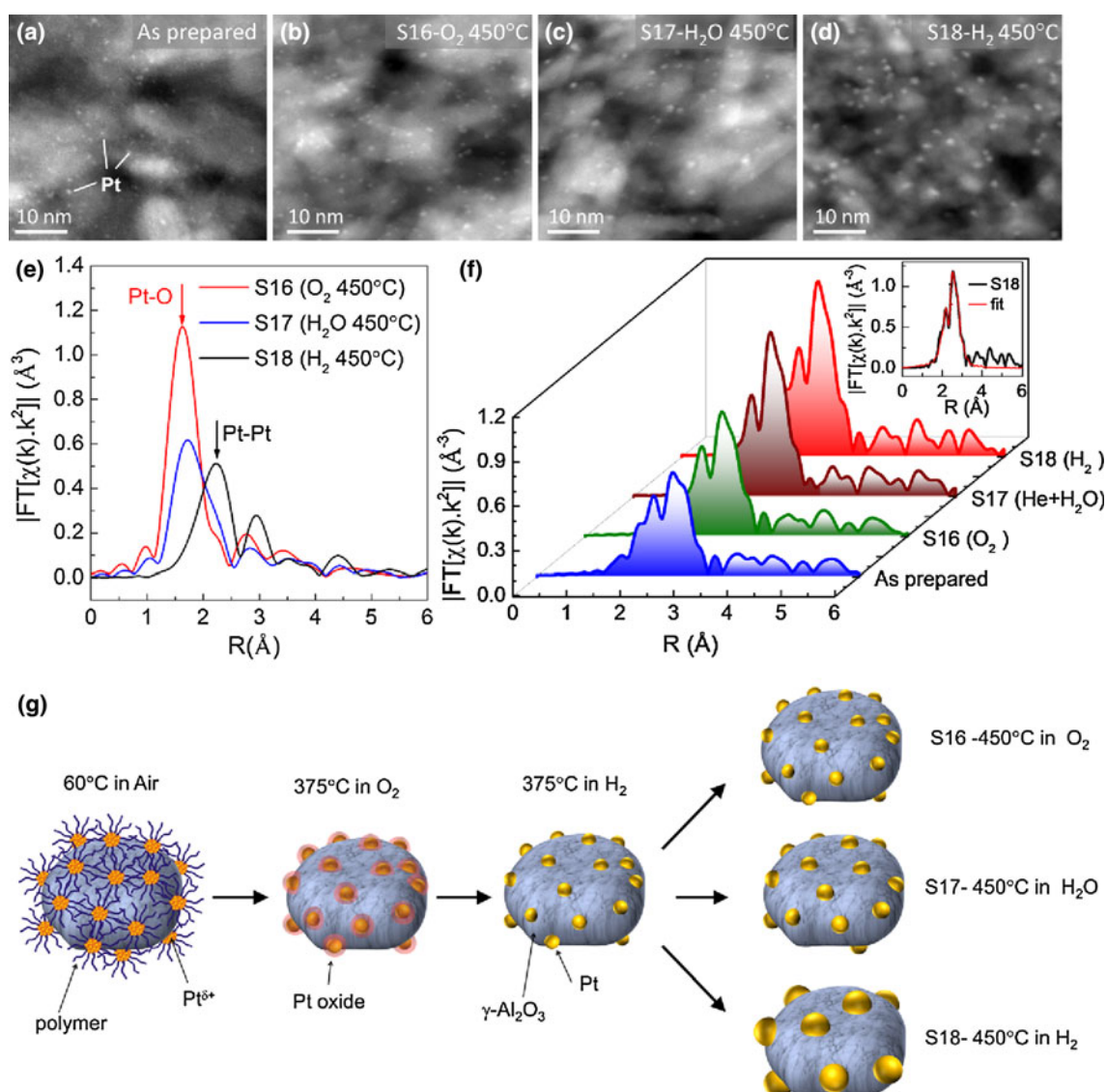
Fig. 8 a–d HAADF-STEM images of Pt NPs supported on γ-Al₂O₃ prepared using an identical micellar NP solution acquired ex situ at room temperature for samples in their as-prepared state (**a**) and after annealing at 450 °C for 3 h in oxygen (S16) (**b**), in H₂O vapor (S17) (**c**), and in hydrogen (S18) (**d**). Fourier transform EXAFS data obtained for S16–S18 in situ during treatments in O₂, H₂O vapor and H₂ at 450 °C (**e**), and on the sample samples after subsequent reduction in H₂ at 375 °C and cooling to room temperature in H₂ (**f**). For comparison, (**f**) also displays EXAFS data from the as-prepared reduced NPs acquired before annealing. The *inset* in (**f**) displays a typical EXAFS spectrum of S18 at RT after the annealing treatment (450 °C in H₂) together with the corresponding single-scattering fit. The schematic model in (**g**) illustrates the behavior of the NPs under the different environments

phenomena have been noticed for Pt/γ-Al₂O₃ after annealing in O₂ below 600 °C [84–93], while treatments at higher temperature resulted in NP sintering [50, 84, 85, 112–114]. Moreover, such effect was only detected in material systems where strong interactions between the oxidized NPs and the oxide support are expected [115–117]. Furthermore, the pre-treatment in O₂ is likely to affect the structure, chemical state, and density of defects on the support surface (i.e. degree of hydroxylation), which are all parameters known to influence the stability of the NPs [10, 118, 119]. For example, adsorbate-induced NP

redispersion phenomena require the detachment of metal oxide species from the NPs and their subsequent migration to trap sites on the support surface. Therefore, defective high surface area supports and low metal loadings are crucial for this effect to occur [120].

Although the experimental results presented above suggest the possible use of pre-treatments in O₂ for the regeneration of coarsened catalysts via redispersion, the possible loss of Pt through the formation of volatile PtOₓ species cannot be overlooked [1]. In the above examples, by comparing the edge jump (Pt-L₃) of S4 before and after

Fig. 9 a High pressure XPS spectra from the Pt-4f core level region of S19 [micelle-synthesized Pt NPs supported on SiO$_2$ (5 nm)/Si (111)] [39] acquired at the given temperatures in H$_2$ (*blue*) and O$_2$ (*red*). After each of the former thermal treatments, XPS spectra were also recorded in H$_2$ at 400 °C (*black*). Thermal evolution of the total Pt-4f XPS peak area (**b**) and Pt-4f$_{7/2}$ binding energy (**c**) in the different chemical environments. AFM images acquired at room temperature before (**d**) and after (**e**) the different annealing cycles in H$_2$/O$_2$ are also shown
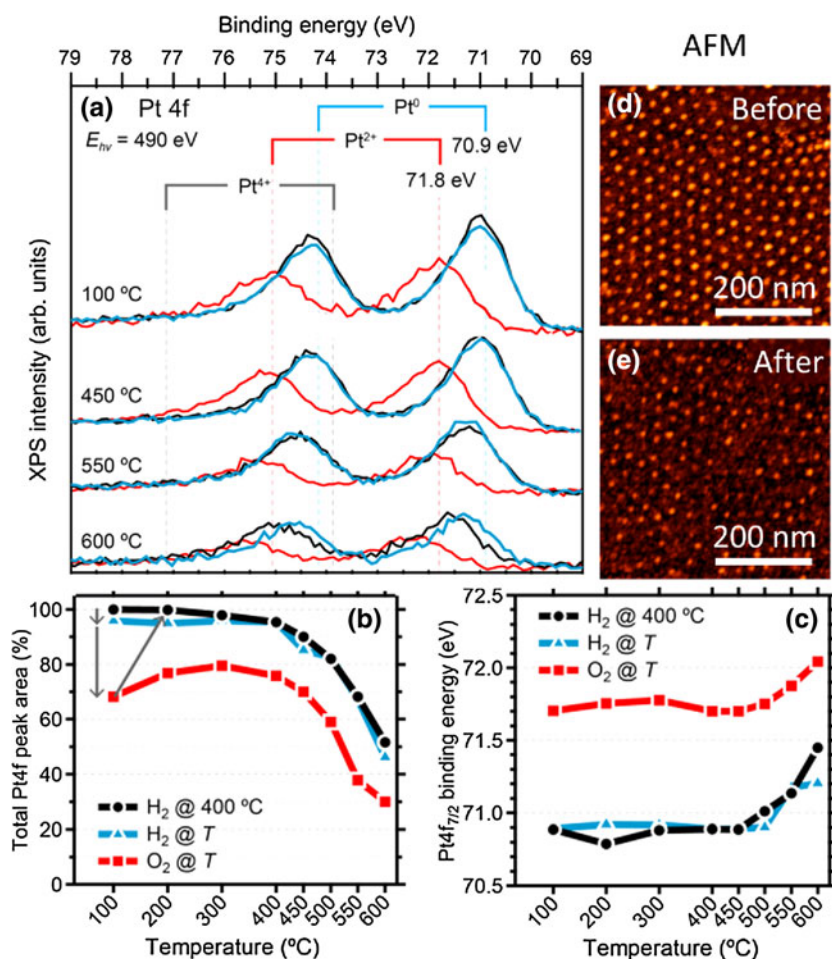
annealing in O$_2$ at 375 °C, no loss of Pt was evidenced. However, such effect cannot be excluded after annealing treatments in O$_2$ at higher temperatures [1]. In addition, the morphology of the support is also expected to play a key role in the stabilization of such volatile species via re-adsorption. Moreover, in the least advantageous cases, sintering could then set in upon the interaction of the initially dispersed NPs with the redispersed and newly readsorbed atoms or cluster fragments.

In order to gain additional insight into the stability of PtO$_x$ species and their role on NP sintering, redispersion or loss of active catalytic material through volatilization, model Pt NP($\sim$2 nm)/SiO$_2$/Si(111) catalysts (S19) were studied in situ under H$_2$ and O$_2$ (0.5 Torr) via ambient pressure XPS [39]. Figure 9a displays Pt-4f XPS spectra from S19 acquired in O$_2$ (red curve) and H$_2$ (blue curve) at the indicated temperatures. Prior to these experiments, the sample was first cleaned by in situ annealing in 0.5 Torr O$_2$ followed by reduction in 0.5 Torr H$_2$ at 400 °C. Subsequently, the sample was measured first in H$_2$ at 400 °C (black), then in H$_2$ at the indicated temperatures (blue) followed by O$_2$ at the same temperatures (red). No significant difference is observed when comparing H$_2$ data

acquired at different temperatures to those measured at 400 °C before each thermal cycle [H$_2$(400 °C)/H$_2$(T)/O$_2$(T) anneal] in terms of binding energy, peak shape and area, Fig. 9b, c. The latter indicates that exclusive annealing in H$_2$ at temperatures above 400 °C does not result in morphological or chemical changes in our samples. Nevertheless, when the annealing step in H$_2$ was followed by an identical treatment in O$_2$ at temperatures ranging from 100 to 600 °C, the subsequent XPS spectra acquired in H$_2$ above $\sim$450 °C were characterized by a higher binding energy and lower spectral area. This result indicates that irreversible changes took place during the O$_2$ exposure. Such changes were not detected when the sample was exposed to H$_2$ at the same temperature. In addition to the decrease in the peak area observed in O$_2$ and in H$_2$ after O$_2$ exposure above $\sim$450 °C, Fig. 9b, significantly larger Pt-4f binding energies (Pt-4f$_{7/2}$ = 71.7–72.0 eV) were measured in O$_2$ as compared to bulk metallic Pt [1, 70, 121–123], Fig. 9c, indicating the formation and stabilization of PtO$_x$ species, in particular, PtO [1, 70, 121, 122]. It should be noted that the lower overall Pt-4f XPS intensities (or peak areas) observed in O$_2$ are due to presence of oxygen atoms in the oxide phase and possibly also to

adsorbate-driven reversible changes in the shape of the Pt NPs in O_2 [124].

The origin of the changes observed in XPS Fig. 9b, c after annealing in O_2 above 450 °C, i.e., the signal attenuation and increase in the metallic Pt (H_2 data) and Pt^{2+} (O_2 data) binding energies point towards the loss of material and decrease of the NP size. In order to corroborate this hypothesis, ruling out possible alternatives such as NP coarsening (which would have also led to a decrease in the spectral area), ex situ AFM images were acquired before and after the in situ XPS experiments, Fig. 9d, e. Lack of NP sintering via diffusion-coalescence was observed, since similar average interparticle distances were measured for these samples before and after the thermal treatment. Nevertheless, despite the strong NP adhesion to the oxide support observed (lack of mobility), a decrease in the average NP from 2.0 ± 0.5 nm in the as-prepared sample to 1.3 ± 0.4 nm in the H_2/O_2 annealed sample was also detected. This result is in good agreement with the predicted final NP height (~ 1 nm) extracted from the Beer-Lambert equation using as input parameters the initial AFM NP height (~ 2 nm) and the change in the XPS intensity (peak area) before and after the thermal treatment [39].

Our data reveal that loss of material, likely in the form of volatile PtO_x species, took place. It is possible that for our system the onset temperature for PtO_x sublimation [125, 126] is lower than the temperature required to overcome the kinetic barrier for PtO_x formation. Accordingly, the immediate desorption of the PtO_x species formed, likely as PtO_2, might have occurred. It is also plausible that the Pt volatilization temperature is dependent on the NP geometry (size, shape and crystalline structure), an aspect that requires additional investigation.

The formation of volatile PtO_x species in oxidizing environments has been previously described [42, 127–129]. Nevertheless, an apparent lack of agreement on their possible involvement in coarsening phenomena can be found in the literature. This is largely due to the different material systems studied (i.e. single crystal vs high surface area porous supports, different initial average NP sizes and interparticle distances, etc.) and distinct experimental conditions (i.e. pure O_2 anneal vs synthetic air, different gas pressures and annealing temperatures). For example, mass loss during O_2 treatments at 500 °C and low pressure ($P_{O2} = 2.3 \times 10^{-4}$ Torr) was observed [128], while an analogous treatment in vacuum revealed NP sintering. On the other hand, others [42, 50, 51, 104, 107] held volatile PtO_x species responsible for coarsening phenomena through the exchange of Pt between adjacent NPs. For instance, coarsening of PVD Pt NPs supported on SiO_2 and Al_2O_3 thin films without apparent loss of Pt was observed via environmental TEM at 7.5 Torr O_2 and 650 °C [50, 51]. In our experiments, the volatile PtO_x species were not

re-deposited on the support, but evacuated by the differential pumping near the sample surface. It should be noted however that under different experimental conditions, for NP systems with broader initial size distributions, more closely-spaced NPs, or on distinct supports (i.e. more porous) such material re-deposition might become significant and might also result in Ostwald-ripening phenomena, which were not observed here.

4 Conclusions

To unravel the complex coarsening behavior of supported NPs, geometrical, chemical, and environmental factors should be taken into account. The present work provides a variety of experimental examples of sintering processes taking place under different gaseous atmospheres, for NPs synthesized using different approaches, with distinct initial average size, shape, dispersion, and support.

In the first section it was shown that the NP synthesis method can play a dominant role in the coarsening rate and pathway through specifics of the resulting NP size, shape, homogeneity, and chemical state (S1–S3). The effect of the interparticle distance was also demonstrated, with larger distances leading to enhanced NP stability against coarsening (S4–S7). For planar samples, a promising approach to reduce sintering is the use of self-assembly synthesis methods, since they guarantee that the NPs are homogenously distributed on the support surface at pre-defined distances (S3–S7, S12–S13, S19). On the other hand, for high surface area powder supports the presence of ligands on the NPs could prevent NP agglomeration during synthesis. On such supports, it was also observed that the larger their surface area, the smaller the NP sintering rate due to the resulting larger interparticle distances and higher barriers for inter-grain (support) diffusion (S8–S11).

The effect of the support material on the coarsening of metal NPs was also illustrated using high surface area (S8–S11) and single crystal substrates (S1–S3, S12–S13). Different metal-support interactions could affect the mobility of NPs and the rate of atom detachment from NPs. Special care should therefore be taken when reducible supports such as TiO_2 or CeO_2 are considered for applications under reducing environments. As it was shown here, the degree of reduction of the support might drastically change the nature and the strength of the NP-support interaction, which in certain cases, such as Pt/TiO_2, could result in the NPs being encapsulated by the support (S12), and in others (Pt/CeO_2) in metal atom diffusion into the support and/or alloy formation (S10). Although a complete encapsulation would hinder NP coarsening, it also prevents the access of reactants to the NP surface, ultimately rendering them useless for catalytic applications.

Our study also describes how the catalyst pretreatment might affect the coarsening behavior of the NPs (S14–S15). For example, a mild annealing treatment in oxygen (~ 350–400 °C) could strongly suppress the subsequent coarsening of NPs under significantly harsher conditions, namely, at 800 °C in H_2 as compared to a similarly annealed sample without such pre-treatment (S14–S15). At last, the effect of the environment on the coarsening behavior of Pt NPs was investigated by comparing three identically prepared Pt/γ-Al_2O_3 samples under O_2, He + H_2O, and H_2 environments at 450 °C (S16–S18). It was shown that for this system, minimum coarsening was achieved under O_2 (S16), followed by He + H_2O (S17). The largest coarsening rate was observed under H_2 (S18). In this case, a direct correlation between the oxidation state of the Pt NPs and their resistance against coarsening was established. Adsorbate-induced coarsening phenomena are relevant to real-world catalytic reactions in which the presence of a variety of adsorbates is inevitable and therefore, a better understanding of these phenomena is of great interest for their industrial utilization. Moreover, it was also shown that in certain environments loss of material could be observed due to the formation of volatile oxide species (S19). For instance, an irreversible decrease in the size of micelle-prepared Pt NPs supported on SiO_2/Si(111) was observed after annealing in O_2 above 450 °C (S19). Such event may occur to a lesser extent on high surface area supports in which the re-deposition and dissociation of the volatile species is more likely. Such re-deposition could be considered as a new coarsening pathway similar to Ostwald ripening but via a gas-phase diffusion pathway instead of the conventional surface-limited atom diffusion.

Finally, it should be stressed that in parallel to direct microscopic and spectroscopic investigations of sintering phenomena such as the ones described in our review, having the ability to model and simulate such processes is key in order to unambiguously determine the specific coarsening pathway. In this regard, further work is needed to improve the physical models describing coarsening processes as well as to incorporate the complexity of real-world catalysts, in particular, the heterogeneous nature of the NP support, and additional environmental effects (stabilizing ligands on the NPs, presence of adsorbates, etc.). Furthermore, more efficient computational methods are yet to be developed to more adequately handle long industrially-relevant time scales. Such effort is ongoing and is expected to lead to great progress in the rational design of novel nanocatalysts with enhanced stability.

References

1. Ono LK, Croy JR, Heinrich H, Roldan Cuenya B (2011) Phys Chem C 115:16856
2. Flores-Camacho JM, Fischer-Wolfarth J-H, Peter M, Campbell CT, Schauermann S, Freund H-J (2011) Phys Chem Chem Phys 13:16800
3. Haruta M (1997) Catal Today 36:153
4. Mavrikakis M, Stoltze P, Norskov JK (2000) Catal Lett 64:101
5. Choudhary TV, Goodman DW (2002) Top Catal 21:25
6. Campbell CT (2004) Science 306:234
7. Ono LK, Sudfeld D, Rolden Cuenya B (2006) Surf Sci 600:5041
8. Croy JR, Mostafa S, Liu J, Sohn YH, Rolden Cuenya B (2007) Catal Lett 118:1
9. Schalow T, Brandt B, Starr DE, Laurin M, Shaikhutdinov SK, Schauermann S, Libuda J, Freund H-J (2007) Phys Chem Chem Phys 9:1347
10. Feng H, Libera JA, Stair PC, Miller JT, Elam JW (2011) ACS Catal 1:665
11. Betta RAD, McCune RC, Sprys JW (1976) Ind Eng Chem Prod Res Dev 15:169
12. Ferreira PJ, la O' GJ, Shao-Horn Y, Morgan D, Makharia R, Kocha S, Gasteiger HAJ (2005) Electrochem Soc 152:A2256
13. Petkovic LM, Ginosar DM, Rollins HW, Burch KC, Deiana C, Silva HS, Sardella MF, Granados D (2009) Int J Hydrogen Energy 34:4057
14. Choudhary VR, Mondal KC, Mamman AS (2005) J Catal 233:36
15. Ginosar DM, Rollins HW, Petkovic LM, Burch KC, Rush MJ (2009) Int J Hydrogen Energy 34:4065
16. Rashkeev SN, Ginosar DM, Petkovic LM, Farrell HH (2009) Catal Today 139:291
17. Petkovic LM, Ginosar DM, Rollins HW, Burch KC, Pinhero PJ, Farrell HH (2008) Appl Catal A 338:27
18. Thomas JM, Thomas WJ (eds) (1997) Principles and practice of heterogeneous catalysis. VCH, Weinheim
19. Veith GM, Lupini AR, Rashkeev S, Pennycook SJ, Mullins DR, Schwartz V, Bridges CA, Dudney NJ (2009) J Catal 262:92
20. Parker SC, Campbell CT (2007) Top Catal 44:3
21. Campbell CT, Parker SC, Starr DE (2002) Science 298:811
22. Parker SC, Campbell CT (2007) Phys Rev B 75:035430
23. Thiel PA, Shen M, Liu D-J, Evans JW (2009) J Phys Chem C 113:5047
24. Ono LK, Rolden Cuenya B (2007) Catal Lett 113:86
25. Behafarid F, Rolden Cuenya B (2012) Surf Sci 606:908
26. Jak MJJ (2000) PhD thesis, Leiden University
27. Jak MJJ, Konstapel C, Van Kreuningen A, Chrost J, Verhoeven J, Frenken JWM (2001) Surf Sci 474:28
28. Jak MJJ, Konstapel C, van Kreuningen A, Verhoeven J, Frenken JWM (2000) Surf Sci 457:295
29. El-Azab A, Gan S, Liang Y (2002) Surf Sci 506:93
30. Matos J, Ono LK, Behafarid F, Croy JR, Mostafa S, DeLaRiva AT, Datye AK, Frenkel AI, Rolden Cuenya B (2012) Phys Chem Chem Phys 14:11457
31. Croy JR, Mostafa S, Heinrich H, Rolden Cuenya B (2009) Catal Lett 131:21
32. Jacobs PW, Ribeiro FH, Somorjai GA, Wind SJ (1996) Catal Lett 37:131
33. Grunes J, Zhu J, Anderson EA, Somorjai GA (2002) J Phys Chem 106:11463
34. Johansson S, Osterlund L, Kasemo B (2001) J Catal 201:275
35. Laurin M, Johanek V, Grant AW, Kasemo B, Libuda J, Freund HJ (2005) J Chem Phys 122:84713
36. Wang SC, Ehrlich G (1990) Surf Sci 239:301

37. Liu CL, Adams JB (1992) Surf Sci 268:73
38. Wen JM, Chang SL, Burnett JW, Evans JW, Thiel PA (1994) Phys Rev Lett 73:2591
39. Porsgaard S, Merte LR, Ono LK, Behafarid F, Matos J, Helveg S, Salmeron M, Rolden Cuenya B, Besenbacher F (2012) ACS Nano. doi:10.1021/nn3040167
40. Smoluchowski MV (1916) Phys Z 17:585
41. Smoluchowski MV (1917) Z Phys Chem 92:129
42. Wynblatt P, Gjostein NA (1975) Prog Solid State Chem 9:21
43. Wynblatt P, Gjostein NA (1976) Acta Metall Mater 24:1165
44. Kandel D (1997) Phys Rev Lett 79:4238
45. Granqvist CG, Duhrman RA (1976) J Catal 42:477
46. Ouyang R, Liu J-X, Li W-XJ (2013) Am Chem Soc. doi:10.1021/ja3087054
47. Datye AK, Xu Q, Kharas KC, McCarty JM (2006) Catal Today 111:59
48. McCarty JG, Malukhin G, Poojary DM, Datye AK, Xu Q (2005) J Phys Chem B 109:2387
49. Goeke RS, Datye AK (2007) Top Catal 46:3
50. Simonsen SB, Chorkendorff I, Dahl S, Skoglundh M, Sehested J, Helveg SJ (2010) J Am Chem Soc 132:7968
51. Simonsen SB, Chorkendorff I, Dahl S, Skoglundh M, Sehested J, Helveg S (2011) J Catal 281:147
52. Mitchell CEJ, Howard A, Carney M, Egdell RG (2001) Surf Sci 490:196
53. Stone P, Poulston S, Bennett RA, Bowker M (1998) Chem Commun 13:1369
54. Lai X, Goodman DW (2000) J Mol Catal A 162:33
55. Starr DE, Shaikhutdinov SK, Freund HJ (2005) Top Catal 36:33
56. Croy JR, Mostafa S, Liu J, Sohn Y, Heinrich H, Rolden Cuenya B (2007) Catal Lett 119:209
57. Kolmakov A, Goodman DW (2001) Surf Sci 490:L597
58. Wahlström E, Lopez N, Schaub R, Thostrup P, Rønnau A, Af-rich C, Lægsgaard E, Nørskov J, Besenbacher F (2003) Phys Rev Lett 90:026101
59. Meli L, Green PF (2008) ACS Nano 2:1305
60. Rolden Cuenya B (2010) Thin Solid Films 518:3127
61. Zhu H, Ma Z, Overbury SH, Dai S (2007) Catal Lett 116:128
62. Ogasawara S, Kato S (2010) J Am Chem Soc 132:4608
63. Wilson OM, Scott RW, Garcia-Martinez JC, Crooks RM (2005) J Am Chem Soc 127:1015
64. Fu B, Missaghi MN, Downing CM, Kung MC, Kung HH, Xiao GM (2010) Chem Mater 22:2181
65. Pileni M-P (2003) Nat Mater 2:145
66. Gabaldon JP, Bore M, Datye AK (2007) Top Catal 44:253
67. Feng H, Lu J, Stair PC, Elam JW (2011) Catal Lett 141:512
68. Rolden Cuenya B (2012) Acc Chem Res. doi:10.1021/ar300226p
69. Naitabdi A, Behafarid F, Rolden Cuenya B (2009) Appl Phys Lett 94:083102
70. Ono LK, Yuan B, Heinrich H, Rolden Cuenya B (2010) J Phys Chem 114:22119
71. Gan S, Liang Y, Baer DR, Grant AW (2001) Surf Sci 475:159
72. Berkó A, Hakkel O, Szökő J, Solymosi F (2002) Surf Sci 507–510:643
73. Alexeev O, Kim D-W, Graham GW, Shelef M, Gates BC (1999) J Catal 185:170
74. Newton MA, Belver-Coldeira C, Martinez-Arias A, Fernandez-Garcia M (2007) Nat Mater 6:528
75. Ingham B, Lim TH, Dotzler CJ, Henning A, Toney M, Tilley RD (2011) Chem Mater 23:3312
76. Chupas PJ, Chapman KW, Jennings G, Lee PL, Grey CPJ (2007) Am Chem Soc Commun 129:13822
77. Asoro MA, Kovar D, Shao-Horn Y, Allard LF, Ferreira PJ (2010) Nanotechnology 21:025701
78. Bartholomew CH (1994) In: Froment GF, Delmon B (eds) Stud Surf Sci Catal, vol 88. Elsevier, Amsterdam, p 1
79. Auvray X, Pingel T, Olsson E, Olsson L (2013) Appl Catal B 129:517
80. Yang J, Tschamber V, Habermacher D, Garin F, Gilot P (2008) Appl Catal B 83:229
81. Nagai Y, Hirabayashi T, Dohmae K, Takagi N, Minami T, Shinjoh H, Matsumoto S (2006) J Catal 242:103
82. Monzón A, Garetto TF, Borgna A (2003) Appl Catal A 248:279
83. Smith DJ, White D, Baird T, Fryer JR (1983) J Catal 81:107
84. Straguzzi GI, Aduriz HR, Gigola CE (1980) J Catal 66:171
85. Lee TJ, Kim YG (1985) Korean J Chem Eng 2:119
86. Weller SW, Montagna AA (1971) J Catal 20:394
87. Fiedorow R (1978) J Catal 51:193
88. Kamiuchi N, Taguchi K, Matsui T, Kikuchi R, Eguchi K (2009) Appl Catal B 89:65
89. Gollob R (1981) J Catal 68:473
90. Johnson MFL, Keith CD (1963) J Phys Chem 67:200
91. Ruckenstein E (1976) J Catal 41:303
92. Fiedorow R, Wanke S (1976) J Catal 43:34
93. Rickard J (1990) J Catal 121:141
94. Fung SC, Tauster SJ, Koo JY (1990) US patent 4925819, 1990
95. Ravel B, Newville M (2005) J Synchrotron Radiat 12:537
96. Newville M (2001) J Synchrotron Radiat 8:322
97. Ravel B, Newville M (2005) Phys Scripta T115:1007
98. Zabinsky S, Rehr J, Ankudinov A, Albers R, Eller M (1995) Phys Rev B 52:2995
99. Fuentes GA, Salinas-Rodríguez E (2001) In: Spivey JJ, Roberts GW, Davis BH (eds) Stud Surf Sci Catal, vol 139. Elsevier, Amsterdam, p 503
100. Benavidez AD, Kovarik L, Genc A, Agrawal N, Larsson EM, Hansen TW, Karim AM, Datye AK (2012) ACS Catal 2:2349
101. Yang WC, Zeman M, Ade H, Nemanich R (2003) Phys Rev Lett 90:136102
102. Yang F, Chen MS, Goodman DW (2009) J Phys Chem C 113:254
103. Liu RJ, Crozier PA, Smith CM, Hucul DA, Blackson J, Salaita G (2004) Microsc Microanal 10:77–85
104. Harris PJF (1995) Int Mater Rev 40:97
105. Sehested J, Gelten JAP, Remediakis IN, Bengaard H, Norskov JK (2004) J Catal 223:432
106. Behafarid F, Rolden Cuenya B (2011) Nano Lett 11:5290
107. Chu Y, Ruckenstein E (1978) J Catal 55:281
108. Graham AJ (1981) J Catal 68:1
109. Kim M-Y, Choi J-S, Toops T, Jeong E-S, Han S-W, Schwartz V, Chen J (2013) J Catal 3:88
110. Susu AA, Ogogo EO, Ngomo HM (2006) Chem Eng Res Des 84:664
111. Ruckenstein E, Chu YF (1979) J Catal 59:109
112. Loof P, Stenbom B, Norden H, Kasemo B (1993) J Catal 144:60
113. Graham GW, Jen HW, Ezekoye O, Kudla RJ, Chun W, Pan XQ, McCabe RW (2007) Catal Lett 116:1
114. Larsson EM, Millet J, Gustafsson S, Skoglundh M, Zhdanov VP, Langhammer C (2012) ACS Catal 2:238
115. Paredis K, Ono LK, Behafarid F, Zhang Z, Yang JC, Frenkel AI, Rolden Cuenya B (2011) J Am Chem Soc 133:13455
116. Lobree LJ, Aylor AW, Reimer JA, Bell AT (1999) J Catal 181:189
117. Okumura K, Niwa M (2000) J Phys Chem B 104:9670
118. Brown MA, Carrasco E, Sterrer M, Freund H-J (2010) J Am Chem Soc 132:4064
119. Jensen MCR, Venkataramani K, Helveg S, Clausen BS, Reichling M, Besenbacher F, Lauritsen JV (2008) J Phys Chem C 112:16953

120. Stulga JE, Wynblatt P, Tien JK (1980) J Catal 62:59
121. Wagner CD, Naumkin AV, Kraut-Vass A, Allison JW, Powell CJ, Rumble JR (2003) NIST X-ray Photoelectron Spectroscopy Database, NIST Standard Reference Database 20, Version 3.5
122. Zhao F, Ikushima Y, Shirai M, Ebina T, Arai M (2002) J Mol Catal A 180:259
123. Puglia C, Nilsson A, Hernnas B, Karis O, Bennich P, Martensson N (1995) Surf Sci 342:119
124. Seriani N, Mittendorfer F (2008) J Phys Condens Mat 20:184023
125. Alcock CB, Hooper GW (1960) Proc R Soc A 254:551
126. Chaston J (1965) Platinum Met Rev 9:51
127. Rubel M, Pszonicka M, Ebel MF, Jabłoński A, Palczewska WJ (1986) J Less Common Met 125:7
128. Lamber R, Romanowski W (1987) J Catal 105:213
129. adysŁaw Romanowski W, Lamber R (1985) Thin Solid Films 127:139
130. Mostafa S, Behafarid F, Croy JR, Ono LK, Li L, Yang JC, Frenkel AI, Rolden Cuenya B (2010) J Am Chem Soc 132:15714